

# NiO/ZnO Nanocomposite as Electrode Material for Supercapacitors

Daolin Zhu, Yijiang Shao\*

Department of Biotechnology, Hefei Technology College, Chaohu 238000, P. R. China

\*E-mail: [shaoyijiang@126.com](mailto:shaoyijiang@126.com)

*Received:* 15 December 2017 / *Accepted:* 4 February 2018 / *Published:* 6 March 2018

---

In this work, NiO/ZnO nanocomposites with different Ni/Zn ratio are grown on nickel foam by a hydrothermal and subsequent calcination process. The nanocomposites have sheet-like morphology, and the size of the nanosheets varies with the change of Ni/Zn ratio. The NiO/ZnO nanocomposites can be used as electrode material for supercapacitors. The specific capacitances of NiO/ZnO nanocomposites are higher than NiO and ZnO alone, and the NiO/ZnO nanocomposites with a Ni/Zn ratio of 3:2 show the highest specific capacitance. This work demonstrates that the construction of binary oxide nanocomposites is a strategy to develop high performance supercapacitor electrode materials.

---

**Keywords:** Hydrothermal synthesis; Nanocomposite; Supercapacitor

## 1. INTRODUCTION

Supercapacitors have received substantial attentions as an energy storage device in recent years. Compared with secondary batteries, supercapacitors have the advantages such as ultrafast charging–discharging rate, wide operation temperature range and very long cycle life [1-10]. Nevertheless, supercapacitors suffer from low specific capacitance and thus low energy density. Such drawbacks limit their potential applications in energy storage area. In order to overcome these drawbacks, researchers have put a lot of works on the development of new types of electrode materials with high performances.

In recent years, transition metal oxides have been widely used as supercapacitor electrode materials. The working principle of transition metal oxides for supercapacitors is based on the fast faradaic redox reactions [11-15]. Compared with carbon materials which work on electrical double-layer mechanism, transition metal oxides can provide higher specific capacitance and thus higher energy density. Apart from single metal oxides, many binary metal oxides have been well studied due

to their richer redox reactions and synergistic effects of the different metal ions. For example, Xiang et al. reported the fabrication of  $\text{NiCo}_2\text{O}_4$  microstructures with different morphologies and their application as electrode materials for supercapacitors [16]; Che and co-workers reported flower-like  $\text{MnCo}_2\text{O}_4$  microstructures for supercapacitor applications [17]; Shen et al. reported a flexible supercapacitor based on  $\text{ZnCo}_2\text{O}_4$  nanorods grown on nickel wires [18]; Wang et al. reported the growth of  $\text{ZnCo}_2\text{O}_4$  nanorod arrays on Ni foam and their utility as supercapacitor electrodes [19]. Although binary metal oxides have drawn intense attentions in the field of supercapacitor, up to now, only spinel structured binary metal oxides are well studied.

In this work, nickel foam supported NiO/ZnO nanocomposites were prepared through a hydrothermal method and subsequent calcination. XRD analysis shows the coexistence of both hexagonal NiO and hexagonal ZnO. SEM observation shows the uniform sheet-like morphology. Electrochemical measurements show that the specific capacitances of the NiO/ZnO nanocomposites are higher than that of the ZnO nanosheets and NiO nanosheets. Furthermore, the influence of Ni/Zn ratio on the electrochemical performances of the NiO/ZnO nanocomposites is also studied. The NiO/ZnO nanocomposites with a Ni/Zn ratio of 3:2 show the highest specific capacitance. This work demonstrates that the binary oxide nanocomposites behave better than single metal oxides, and have potential applications for high-performance supercapacitors.

## 2. EXPERIMENTAL SECTION

### 2.1 Materials

Zinc chloride hexahydrate ( $\text{Zn}(\text{NO}_3)_2 \cdot 6\text{H}_2\text{O}$ ), nickel chloride hexahydrate ( $\text{Ni}(\text{NO}_3)_2 \cdot 6\text{H}_2\text{O}$ ), urea ( $\text{CO}(\text{NH}_2)_2$ ) and potassium hydroxide (KOH) were purchased from Sinopharm Chemical Reagent Co. with analytical grade and used without further purification. Deionized water was used throughout.

### 2.2 Synthesis procedure

**Table 1.** The dosage of reagents used for the preparation of precursors, the corresponding final sample name and mass loading of final samples on nickel foam.

Precursor name	$n(\text{Ni}^{2+})$ (mmol)	$n(\text{Zn}^{2+})$ (mmol)	$n(\text{urea})$ (mmol)	Final sample name	Final mass loading ( $\text{mg cm}^{-2}$ )
Pre-1	1.6	0.4	4	NiZn-1	2.1
Pre-2	1.2	0.8	4	NiZn-2	2.3
Pre-3	0.8	1.2	4	NiZn-3	2.6
Pre-4	2	0	4	NiO	1.7
Pre-5	0	2	4	ZnO	2.7

The dosage of reagents used for the preparation of precursors are listed in Table 1. Take pre-1 as an example, in a typical procedure, metal salts and urea were dissolved in 40 mL deionized water

under constant stirring. Then the solution was transferred into a Teflon-lined stainless-steel autoclave with a capacity of 60 mL. A piece of nickel foam with a size of 2 cm × 3 cm which had been washed with ethanol, 3 mol L<sup>-1</sup> hydrochloric acid and deionized water were immersed in sequence in the solution. The autoclave was sealed, and then heated in an oven at 120 °C for 6 h. After cooled down to room temperature naturally, the nickel foam was collected and washed with deionized water for several times, then dried in vacuum at 50 °C for 3 h. The precursor loaded nickel foam was heated under ambient atmosphere in a muffle furnace at 400 °C for 2 h to obtain the final products. The mass of each final sample on nickel foam was determined by weighing the nickel foam before and after the synthesis process, and listed in Table 1.

### 2.3 Characterizations

Morphologies of the as-prepared samples were observed with field emission scanning electron microscope (FE-SEM, Hitachi S-4800). X-ray powder diffraction (XRD) patterns were obtained on a Bruker D8 Advance diffractometer with Cu K $\alpha$  radiation. X-ray photoelectron spectroscopies (XPS) were recorded on an ESCALab MKII spectrometer with Mg K $\alpha$  radiation.

### 2.4 Electrochemical measurements

The electrochemical performances of as-prepared samples were measured with a three-electrode cell at room temperature. The nickel foams loaded with final samples were cut into 1 cm × 1 cm size and were directly used as the working electrodes. A mercuric oxide electrode and a platinum plate were used as the reference electrode and the counter electrode, respectively. A 3 mol L<sup>-1</sup> KOH solution acted as the electrolyte. Cyclic voltammetry (CV) and galvanostatic charge-discharge (GCD) measurements were performed on a CHI-660E electrochemical working station (Chenhua Corp., Shanghai, China). The specific capacitance ( $C_s$ ) can be evaluated according to the following equations: [20]

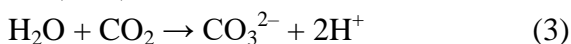
$$C_s = (I\Delta t)/(m\Delta V) \quad (1)$$

The  $C_s$ ,  $I$ ,  $\Delta t$ ,  $m$ ,  $S$ ,  $\Delta V$  represent the specific capacitance, areal capacitance, discharging current, discharging time, active mass, electrode geometrical area and the potential window.

## 3. RESULTS AND DISCUSSION

### 3.1 Composition and morphology characterization

The NiO/ZnO nanocomposites were prepared through two steps. In the first step, the hydrolysis of urea under hydrothermal condition released ammonia and carbon dioxide, and then, Ni<sup>2+</sup> and Zn<sup>2+</sup> can be co-precipitated. The following reactions may occur.



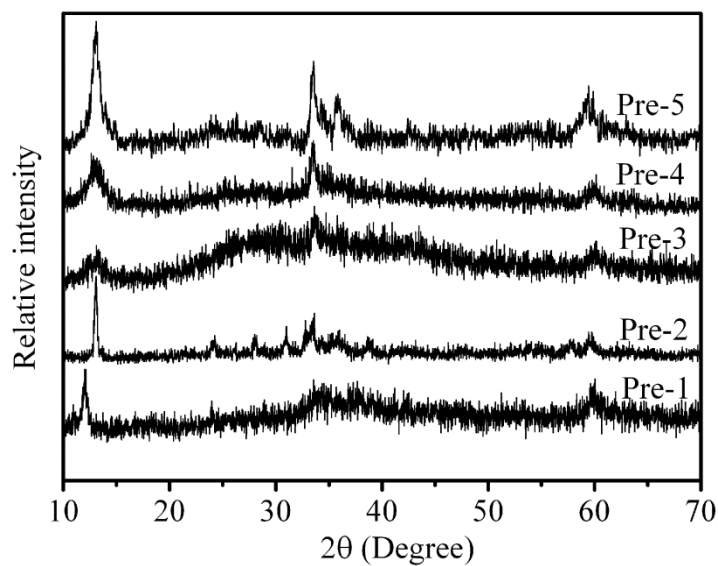
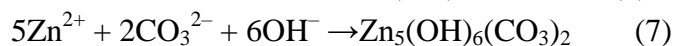
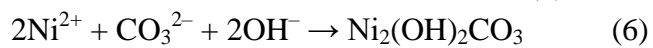
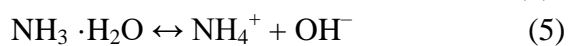
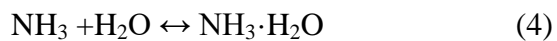


**Figure 1.** XRD patterns of the precursors.

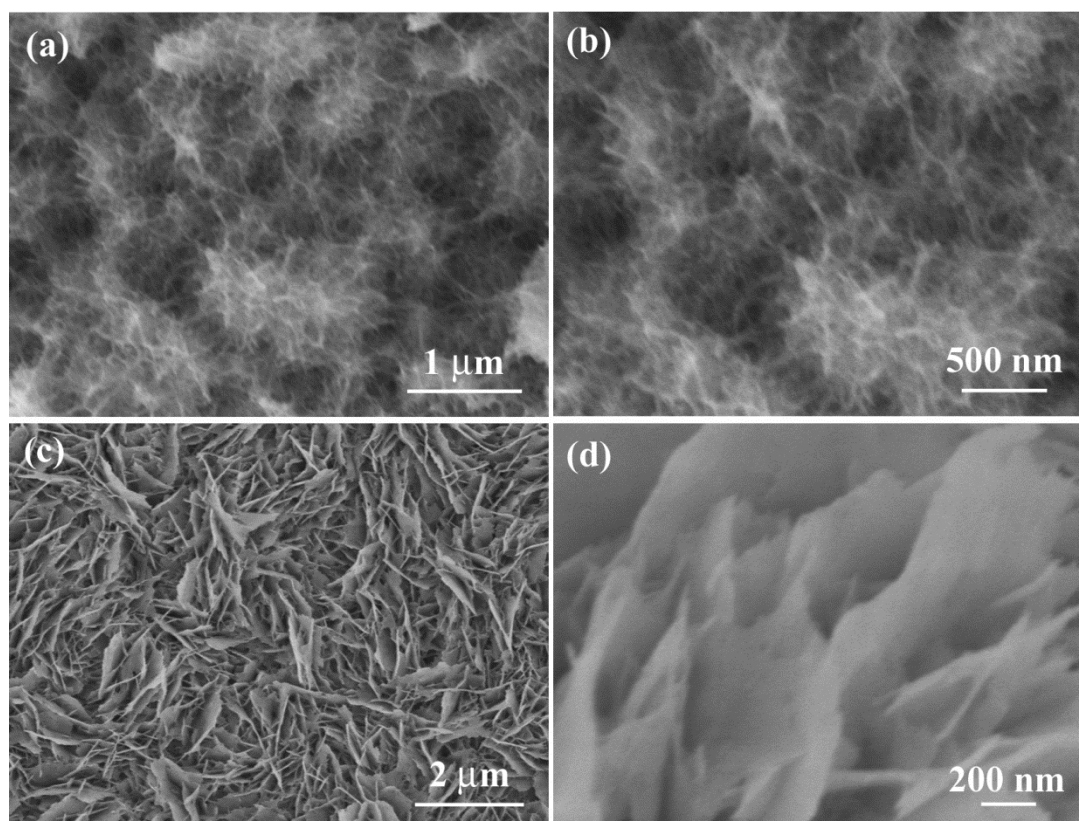


**Figure 2.** SEM images of the pre-4 (a,b) and pre-5 (c,d) samples.

Fig.1 shows typical XRD patterns of the precursors separated from nickel foam by ultrasonication. The XRD pattern of the precursor (pre-4) prepared from  $\text{Ni}^{2+}$  and urea can be indexed to monoclinic phase  $\text{Ni}_2(\text{OH})_2\text{CO}_3 \cdot \text{H}_2\text{O}$  (JCPDS 38-0714), and the XRD pattern of the precursor (pre-5) prepared from  $\text{Zn}^{2+}$  and urea can be indexed to monoclinic phase  $\text{Zn}_5(\text{OH})_6(\text{CO}_3)_2$  (JCPDS 72-1100). The other precursors which were prepared from  $\text{Ni}^{2+}$ ,  $\text{Zn}^{2+}$  and urea can be indexed to a mixture of  $\text{Ni}_2(\text{OH})_2\text{CO}_3 \cdot \text{H}_2\text{O}$  and  $\text{Zn}_5(\text{OH})_6(\text{CO}_3)_2$ .

The morphologies of the precursors are observed by SEM. Fig. 2a and 2b show typical SEM images of the  $\text{Ni}_2(\text{OH})_2\text{CO}_3 \cdot \text{H}_2\text{O}$  (pre-4) sample, which display that the pre-4 sample is composed of many ultrathin nanosheets. Fig. 2c and 2d show representative SEM images of the  $\text{Zn}_5(\text{OH})_6(\text{CO}_3)_2$  (pre-5) sample. This sample is also composed of many nanosheets. However, these nanosheets are obviously larger and thicker than the pre-4 sample.

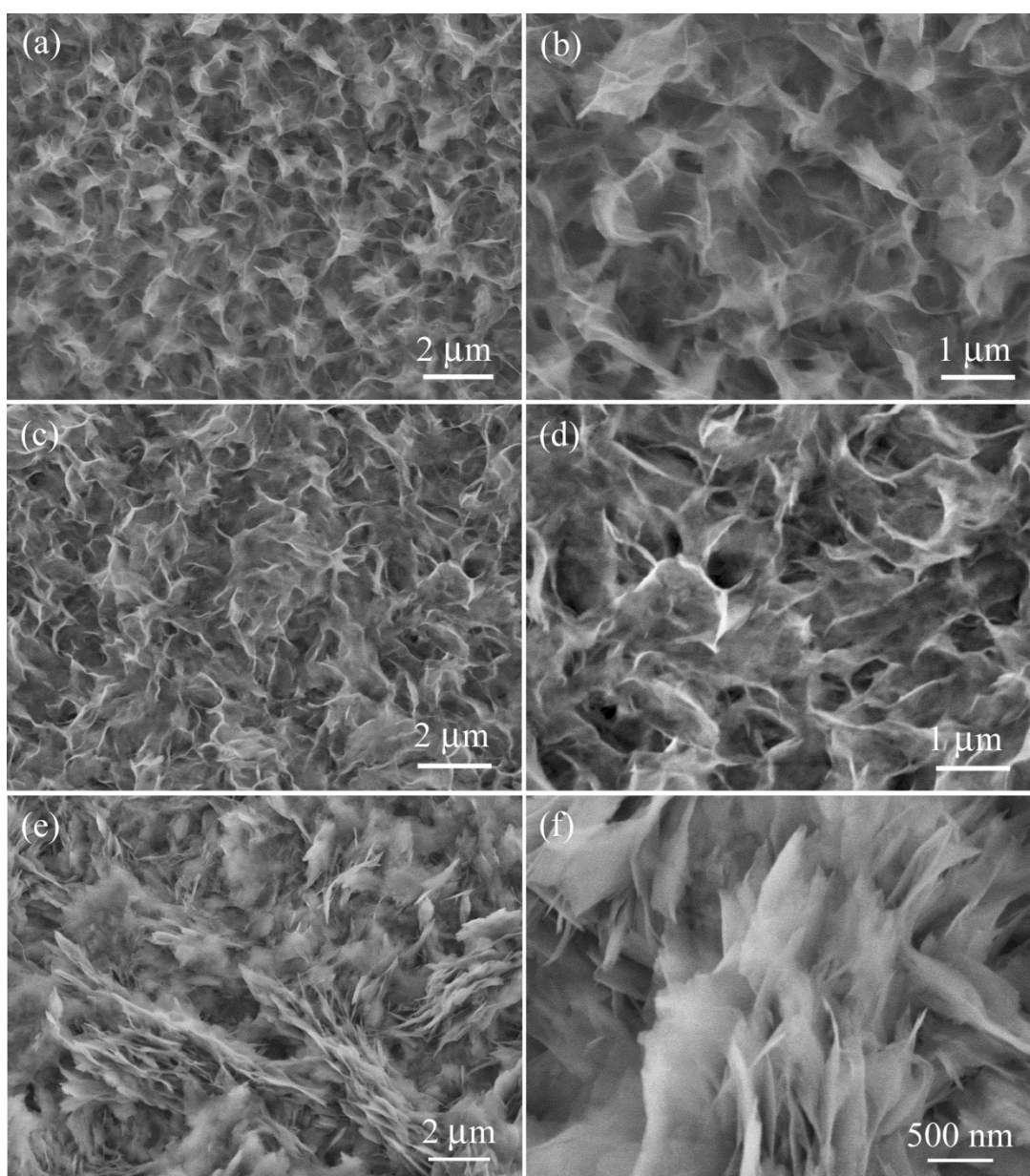


**Figure 3.** SEM images of the pre-1 (a,b), pre-2 (c,d) and pre-3 (e,f) samples.

SEM images of the precursors obtained with different Ni/Zn ratio are presented in Fig. 3. These precursors also take on nanosheet morphology. With the decrease of Ni/Zn ratio in the precursors, the nanosheets tend to be larger and thicker. SEM images (Fig. 3e and 3f) of the pre-3 sample are very similar to that of the  $\text{Zn}_5(\text{OH})_6(\text{CO}_3)_2$  sample. Furthermore, the morphologies of these precursors are uniform, indicating that the  $\text{Zn}_5(\text{OH})_6(\text{CO}_3)_2$  and  $\text{Ni}_2(\text{OH})_2\text{CO}_3 \cdot \text{H}_2\text{O}$  may grown in a whole part.

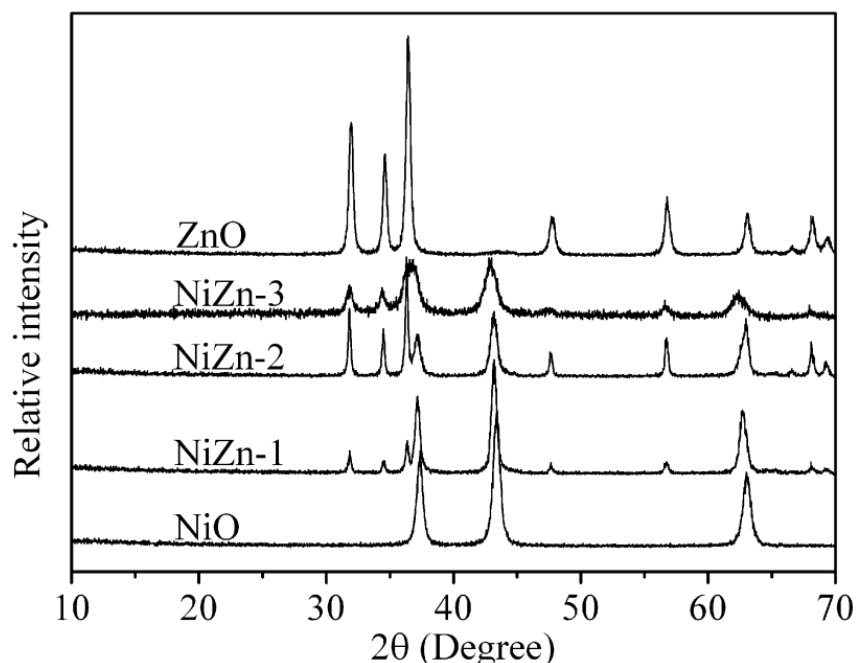


**Figure 4.** XRD patterns of the final samples.

The precursors were further calcined at 400 °C in air for 2 h to obtain the final samples. During the calcination process, the basic carbonates would decompose and finally convert into oxides. The composition of the final samples is characterized by XRD, as shown in Fig. 4. XRD patterns of the samples converted from pre-4 and pre-5 can be indexed to hexagonal NiO (JCPDS no. 47-1049) and hexagonal ZnO (JCPDS 75-0576), respectively. The XRD patterns of the NiZn-1, NiZn-2 and NiZn-3 samples which were calcined from pre-1, pre-2 and pre-3 samples show both diffraction peaks from NiO and ZnO. With the decrease of Ni/Zn ratio, the intense of the diffraction peaks from NiO decreases while the intense of the diffraction peaks from ZnO increases. XRD results indicate that the NiZn-1, NiZn-2 and NiZn-3 samples are composed of NiO and ZnO.

SEM images of the final samples are shown in Fig. 5. As the final samples are obtained from the precursors by calcination in air, the shapes of the precursors are retained well, as can be indicated from the SEM images. However, different from the smooth surfaces of the precursors, all the final samples are porous. The porous structure of the final samples is formed due to the volume shrinkage as well as the release of gaseous species during the calcining process.

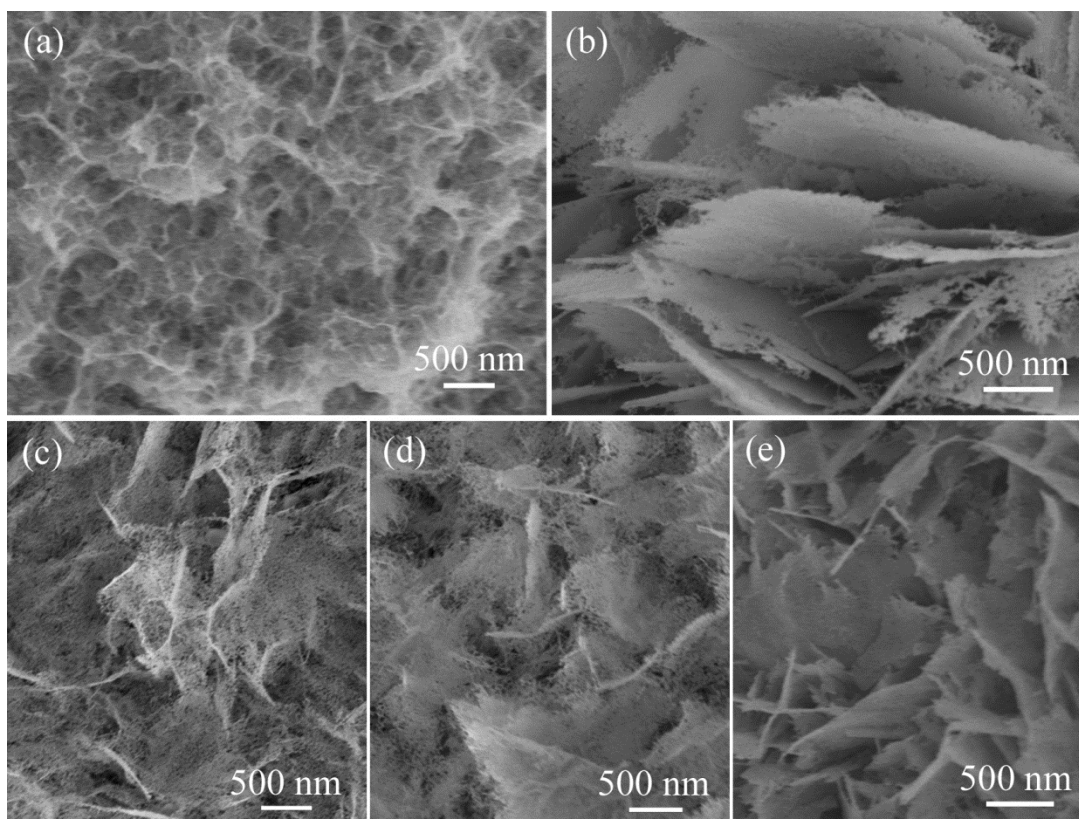


**Figure 5.** SEM images of the final samples: (a) NiO, (b) ZnO, (c) NiZn-1, (d) NiZn-2 and (e) NiZn-3.

Take the NiZn-1 sample as an example, the elemental composition and oxidation state of the NiO/ZnO nanocomposite is analyzed by X-ray photoelectron spectroscopy (XPS). Fig. 6a shows a survey spectrum from 0 to 1100 eV. The peaks located at 531, 856 and 1022 eV correspond to O 1s, Ni 2p and Zn 2p, respectively. The C 1s (as reference) can be attributed to the surface absorption of carbon dioxide in air. The survey spectrum reveals the existence of O and Ni and Zn elements in the sample. High resolution XPS spectra of the Ni, Zn and O elements are shown in Fig. 6b–d. These peaks are computer fitted by using a Gaussian fitting method. Fig. 6b shows the high resolution XPS spectrum of the Ni 2p region. The Ni 2p<sub>3/2</sub> at 855.6 eV, Ni 2p<sub>1/2</sub> at 873.4 eV and two shake-up satellites can be clearly seen. The Ni 2p peak positions are close to the characteristic peaks of Ni<sup>2+</sup> [21]. Furthermore, the Ni 2p peaks cannot be fitted into more peaks, indicating that only Ni<sup>2+</sup> cations present in the sample. Fig. 6c shows the high resolution XPS spectrum of the Zn 2p region. The Zn 2p<sub>3/2</sub> at 1045.1 eV and Zn 2p<sub>1/2</sub> at 1022.2 eV can be clearly seen, and consistent with the reported values of Zn<sup>2+</sup> [19]. Similar to the Ni 2p peaks, the Zn 2p peaks cannot be fitted into more peaks, revealing that only Zn<sup>2+</sup> cations exist in the sample. High resolution XPS spectrum of O 1s is shown in Fig. 6d. This peak can be fitted into three peaks located at 529.3, 530.6 and 531.9 eV, respectively. The peak at 529.3 eV can be attributed to the metal–oxygen bonds [22], the peak at 530.6 eV can be attributed to hydroxyl species from surface adsorbed water [23], and the peak at 531.9 eV come from oxygen ions in low coordination at the surface [24]. From the above results, it can be concluded that the NiZn-1 sample is composed of Ni<sup>2+</sup>, Zn<sup>2+</sup> and O<sup>2-</sup>.

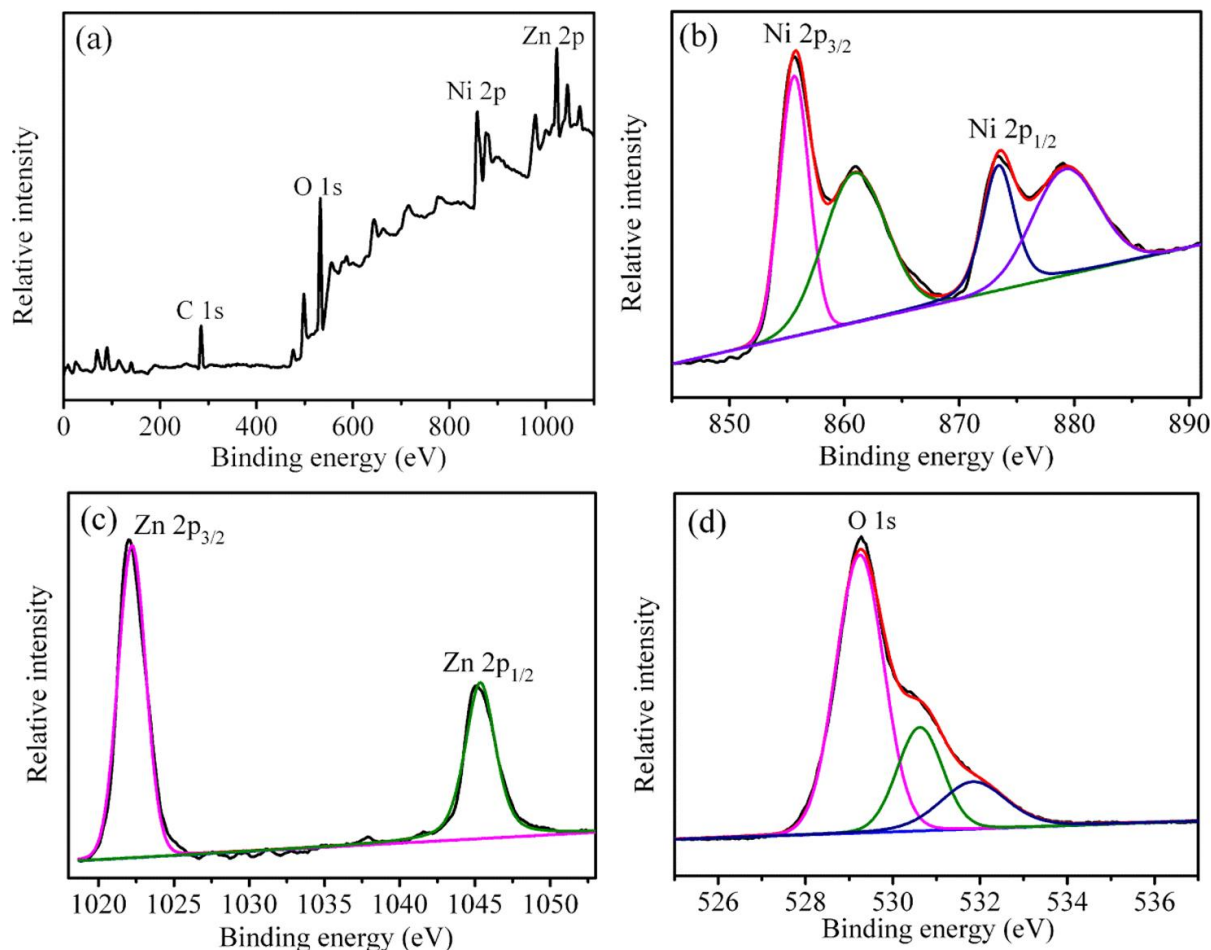


**Figure 6.** XPS spectra of the NiZn-2 sample: (a) survey, (b) Ni 2p, (c) Zn 2p and (d) O 1s.

### 3.2 Characterization of electrochemical properties

The electrochemical performances of the NiO/ZnO nanocomposites with different Ni/Zn ratio are systematically evaluated by CV and GCD measurements performed in a three electrode cell at room temperature. For comparison, the electrochemical performances of the NiO and ZnO porous nanosheets are also evaluated. Fig. 7a shows CV curves of the NiO, ZnO and NiZn-2 samples in a potential range of 0 to 0.6 V at a scan rate of 10 mV s<sup>-1</sup>. All of the CV curves show obvious redox peaks, indicating the occurrence of the faradaic redox reactions during the scan process [25-30]. It is obvious that the integral area of the CV curve of NiZn-2 sample is larger than those of the ZnO and NiO samples. This result implies that the specific capacitance of NiZn-2 sample is higher than the NiO and ZnO samples. Fig. 7b shows CV curves of the NiZn-1, NiZn-2 and NiZn-3 samples at a scan rate of 10 mV s<sup>-1</sup>. Obvious redox peaks can be seen in these CV curves, showing pseudocapacitance features of these electrode materials.

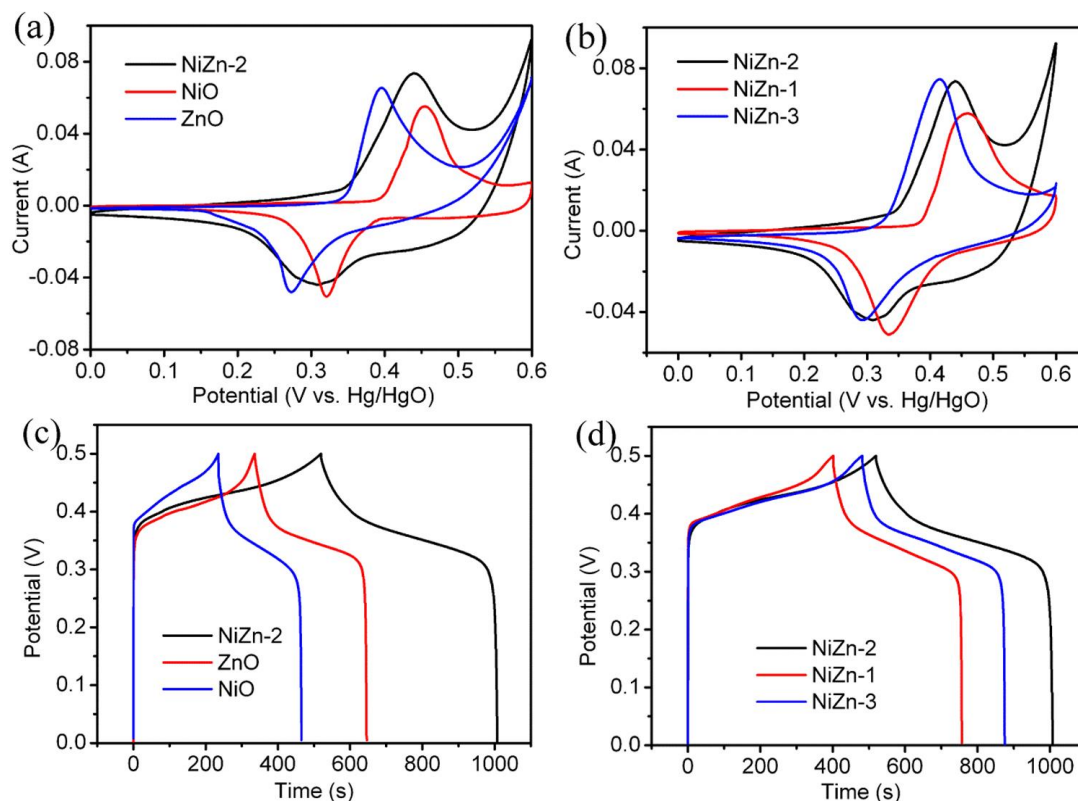


**Figure 7.** (a) CV curves of NiO, ZnO and NiZn-2 samples at a scan rate of  $10 \text{ mV s}^{-1}$ ; (b) CV curves of NiZn-1, NiZn-2 and NiZn-3 samples at a scan rate of  $10 \text{ mV s}^{-1}$ ; (c) GCD curves of NiO, ZnO and NiZn-2 samples at a current density of  $1 \text{ A g}^{-1}$ ; (d) GCD curves of NiZn-1, NiZn-2 and NiZn-3 samples at a current density of  $1 \text{ A g}^{-1}$ .

Fig. 7c shows GCD curves of the NiO, ZnO and NiZn-2 samples measured at a current density of  $1 \text{ A g}^{-1}$  in a potential window of 0 to 0.5 V. It is obvious that the discharging time of NiZn-2 sample is the longest among the three samples. The specific capacitances of the as-synthesized samples are calculated from the discharging time based on equation (1). The specific capacitances of the NiO, ZnO and NiZn-2 samples are  $458$ ,  $620$  and  $976 \text{ F g}^{-1}$ , respectively. Fig. 7d shows GCD curves of the NiZn-1, NiZn-2 and NiZn-3 samples at  $1 \text{ A g}^{-1}$ . The specific capacitances of these samples calculated from these curves are  $710$ ,  $976$  and  $788 \text{ F g}^{-1}$ , respectively. The results indicate that all the NiO/ZnO nanocomposites have higher specific capacitances than NiO and ZnO, and the NiZn-2 sample with a Ni/Zn ratio of 3:2 shows the highest specific capacitance among the NiO/ZnO nanocomposites.

Fig. 8a shows a series of CV curves of the NiZn-2 sample at different scan rates ranging from  $10$  to  $80 \text{ mV s}^{-1}$  in a potential range of 0 to 0.6 V. In all these CV curves, a pair of redox peaks can be clearly seen, indicating the good reversibility of the redox reactions[27]. With the increase of scan rates, the redox peaks gradually move to more negative and positive positions. Fig. 8b shows a series of GCD curves of the NiZn-2 sample at different current densities. The specific capacitances of the NiZn-2 sample are  $976$ ,  $936$ ,  $904$ ,  $795$  and  $723 \text{ F g}^{-1}$  at the current densities of  $1$ ,  $2$ ,  $4$ ,  $8$  and  $16 \text{ A g}^{-1}$ , respectively, as shown in Fig. 8c. The capacitance at  $16 \text{ A g}^{-1}$  is 74.1% of the value at  $1 \text{ A g}^{-1}$ . This result shows a good rate capability of the electrode material. The cycling stability of the NiZn-2

sample was tested at a current density of  $4 \text{ A g}^{-1}$  for 3000 cycles, as shown in Fig. 8d. The specific capacitance decreased gradually upon cycling. After 3000 charging–discharging cycles, the capacitance retention is 78.5%, revealing a good cycling stability.

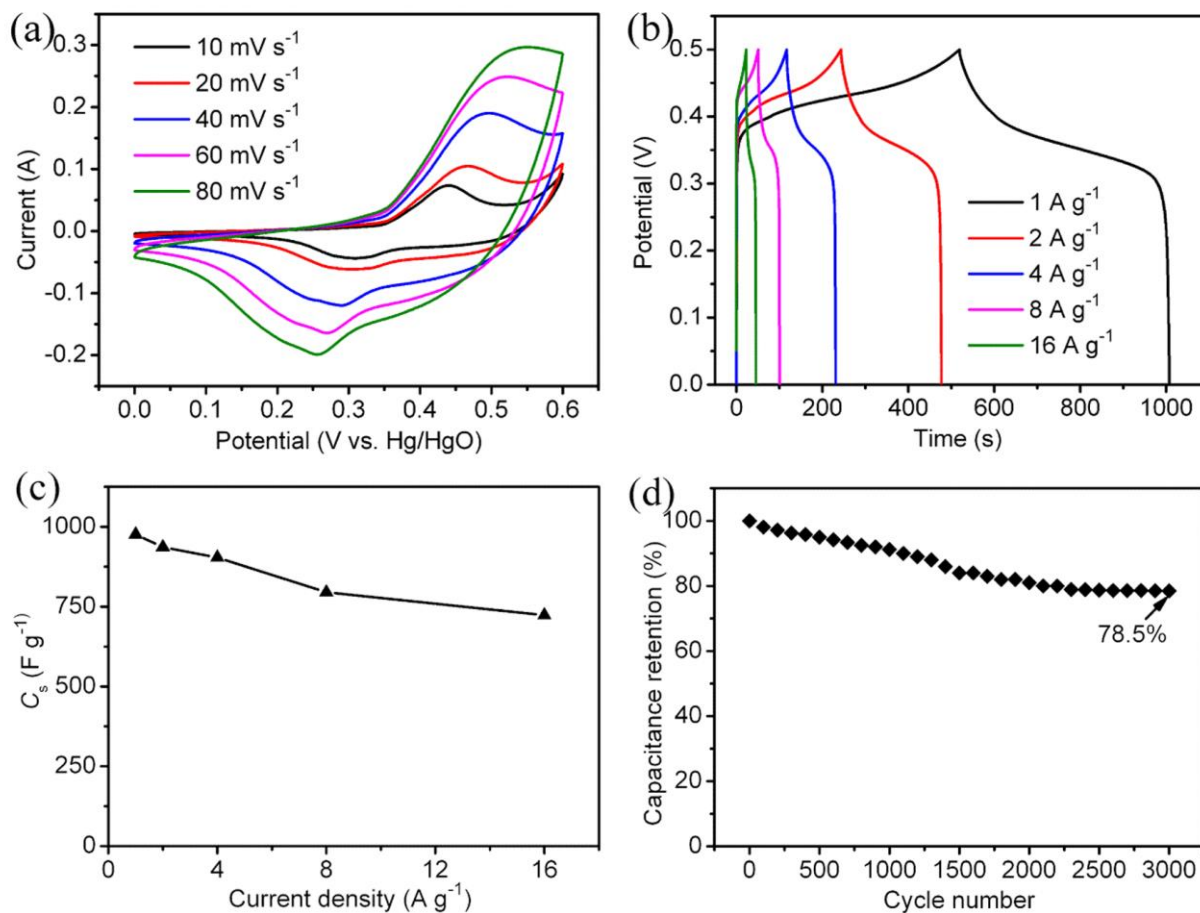


**Figure 8.** CV curves of NiZn-2 sample at different scan rates; (b) GCD curves of NiZn-2 sample at different current densities; (c) specific capacitances of NiZn-2 sample at different current densities; (d) capacitance retention of NiZn-2 sample vs. cycle number.

The higher capacitances of the NiZn-2 sample than NiO and ZnO may be according to the following reasons. First, the NiO/ZnO nanocomposites contain two kinds of cations, therefore the faradaic redox behavior is richer than NiO and ZnO. Second, more ion channels would be provided by the crystal defects presented in the NiO/ZnO nanocomposites, thus the quasi two-dimensional area of faradaic redox reactions can be expanded.

#### 4. CONCLUSIONS

In summary, NiO/ZnO nanocomposites with different Ni/Zn ratio are successfully synthesized by a hydrothermal and subsequent calcination process. The composition and morphologies of the

samples are characterized by XRD and SEM. The nanocomposites take on porous nanosheet morphology, which is suitable for application as an electrode material for supercapacitor. The specific capacitances of the NiO/ZnO nanocomposites are higher than NiO and ZnO nanosheets, and the NiO/ZnO nanocomposites with a Ni/Zn ratio of 3:2 show the highest specific capacitance. This work demonstrates that the construction of binary oxide nanocomposites is an effective way to develop supercapacitor electrode materials with excellent electrochemical performances.

## References

1. B. E. Conway, *J. Electrochem. Soc.*, 138 (1991) 1539.
2. B. E. Conway, V. Birss, J. Wojtowicz, *J. Power Sources*, 66 (1997) 1.
3. A. S. Arico, P. Bruce, B. Scrosati, J. M. Tarascon, W. Van Schalkwijk, *Nat. Mater.*, 4 (2005) 366
4. P. Simon, Y. Gogotsi, *Nat. Mater.*, 7 (2008) 845.
5. J. Yan, Z. Fan, W. Sun, G. Ning, T. Wei, Q. Zhang, R. Zhang, L. Zhi, F. Wei, *Adv. Funct. Mater.*, 22 (2012) 2632.
6. I. E. Rauda, V. Augustyn, B. Dunn, S. H. Tolbert, *Acc. Chem. Res.*, 46 (2013) 1113.
7. S. H. Aboutalebi, R. Jalili, D. Esrafilzadeh, M. Salari, Z. Gholamvand, S. Aminorroaya Yamini, K. Konstantinov, R. L. Shepherd, J. Chen, S. E. Moulton, P. C. Innis, A. I. Minett, J. M. Razal, G. G. Wallace, *ACS Nano*, 8 (2014) 2456.
8. V. Augustyn, P. Simon, B. Dunn, *Energy Environ. Sci.*, 7 (2014) 1597.
9. X. Peng, L. Peng, C. Wu, Y. Xie, *Chem. Soc. Rev.*, 43 (2014) 3303.
10. X. Wang, B. Liu, R. Liu, Q. Wang, X. Hou, D. Chen, R. Wang, G. Shen, *Angew. Chem. Inter. Ed.*, 53 (2014) 1849.
11. L. Cui, L. Huang, M. Ji, Y. Wang, H. Shi, Y. Zuo, S. Kang, *J. Power Sources*, 333 (2016) 118.
12. G. Meng, Q. Yang, X. Wu, P. Wan, Y. Li, X. Lei, X. Sun, J. Liu, *Nano Energy*, 30 (2016) 831.
13. L. Zhang, W. Zheng, H. Jiu, C. Ni, J. Chang, G. Qi, *Electrochim. Acta*, 215 (2016) 212.
14. Z. Zhang, H. Zhang, X. Zhang, D. Yu, Y. Ji, Q. Sun, Y. Wang, X. Liu, *J. Mater. Chem. A*, 4 (2016) 18578.
15. K. Chi, Z. Zhang, Q. Lv, C. Xie, J. Xiao, F. Xiao, S. Wang, *ACS Appl. Mater. Inter.*, 9 (2017) 6044.
16. N. Xiang, Y. Ni, X. Ma, *Chem. Asian J.*, 10 (2015) 1972.
17. H. W. Che, Y. Q. Wang, Y. X. Mao, *J. Alloy. Compd.*, 680 (2016) 586.
18. B. Liu, B. Liu, Q. Wang, X. Wang, Q. Xiang, D. Chen, G. Shen, *ACS Appl. Mater. Inter.*, 5 (2013) 10011.
19. S. Wang, J. Pu, Y. Tong, Y. Cheng, Y. Gao, Z. Wang, *J. Mater. Chem. A*, 2 (2014) 5434.
20. X. Z. Wang, Y. H. Xiao, D. C. Su, L. M. Zhou, S. D. Wu, L. F. Han, S. M. Fang, S. K. Cao, *Electrochim. Acta*, 194 (2016) 377.
21. Y. Zhang, L. Zuo, L. Zhang, J. Yan, H. Lu, W. Fan, T. Liu, *Nano Res.*, 9 (2016) 2747.
22. T. Choudhury, S. O. Saied, J. L. Sullivan, A. M. Abbot, *J. Phys. D Appl. Phys.*, 22 (1989) 1185.
23. Y. E. Roginskaya, O. V. Morozova, E. N. Lubnin, Y. E. Ulitina, G. V. Lopukhova, S. Trasatti, *Langmuir*, 13 (1997) 4621.
24. V. M. Jiménez, A. Fernández, J. P. Espinós, A. R. González-Elipe, *J. Electron Spectrosc.*, 71 (1995) 61.
25. Ü. Alver, A. Tanrıverdi, Ö. Akgül, *Synthetic Met.*, 211 (2016) 30.
26. G. Huang, W. Zhang, S. Xu, Y. Li, Y. Yang, *Ionics*, 22 (2016) 2169.
27. G. C. Li, P. F. Liu, R. Liu, M. Liu, K. Tao, S. R. Zhu, M. K. Wu, F. Y. Yi, L. Han, *Dalton T.*, 45 (2016) 13311.
28. S. Wu, K.S. Hui, K.N. Hui, K.H. Kim, *J. Mater. Chem. A*, 4 (2016) 9113.

29. Y. Han, S. Zhang, N. Shen, D. Li, X. Li, *Mater. Lett.*, 188 (2017) 1.
30. J. Zhao, H. Liu, Q. Zhang, *Appl. Surf. Sci.*, 392 (2017) 1097.

© 2018 The Authors. Published by ESG ([www.electrochemsci.org](http://www.electrochemsci.org)). This article is an open access article distributed under the terms and conditions of the Creative Commons Attribution license (<http://creativecommons.org/licenses/by/4.0/>).